Surface-conductivity enhancement of PMMA by keV-energy metal-ion implantation

M.E. Bannister, H.Hijazi, H.M. Meyer III, V. Cianciolo, and F.W. Meyer[1]
Oak Ridge National Laboratory, Oak Ridge, Tennessee, USA 37831-6372

Abstract

An experiment has been proposed to measure the neutron electric dipole moment (nEDM) with high precision at the Oak Ridge National Laboratory (ORNL) Spallation Neutron Source. One of the requirements of this experiment is the development of PMMA (Lucite) material with a sufficiently conductive surface to permit its use as a high-voltage electrode while immersed in liquid He. At the ORNL Multicharged Ion Research Facility, an R&D activity is under way to achieve suitable surface conductivity in poly-methyl methacrylate (PMMA) using metal ion implantation. The metal implantation is performed using an electron-cyclotron-resonance (ECR) ion source and a recently developed beam line deceleration module that is capable of providing high flux beams for implantation at energies as low as a few tens of eV. The latter is essential for reaching implantation fluences exceeding $1x10^{16}cm^{-2}$, where typical percolation thresholds in polymers have been reported. In this contribution, we report results on initial implantation of Lucite by Ti and W beams with keV energies to average fluences in the range 0.5 – 6.2 x 10^{16} cm^{-2}. Initial measurements of surface-resistivity changes are reported as function of implantation fluence, energy, and sample temperature. We also report x-ray photoelectron spectroscopy (XPS) surface and depth profiling measurements of the ion implanted samples, to identify possible correlations between the near surface and depth resolved implanted W concentrations and the measured surface resistivities.

Keywords: surface conductivity, metal-ion implantation, polymer, tungsten

I. INTRODUCTION

Seeking to understand the mechanism responsible for the production of matter in the aftermath of the Big Bang, researchers have proposed an experiment, known as nEDM [Golub, 1994], to measure the neutron electric dipole moment with unprecedented precision at the Spallation Neutron Source (SNS) Fundamental Neutron Physics Beamline. One of the technical issues that must be addressed in the experiment design is the development of high-voltage electrodes for the nEDM experiment that must satisfy several challenging and unique materials criteria. To collect the scintillation signals produced by neutron/He-3 capture events, the measurement cell and high-voltage electrodes both must be constructed of poly-methyl methacrylate (PMMA) since it has high optical clarity and will not be significantly activated by the ambient neutron flux. In order to reach the desired sensitivity, these electrodes must be capable of sustaining electric fields up to 75 kV/cm across an 8-cm gap filled with liquid He. Since the acrylic is not a conductor, the electrode surfaces must be made conducting; one possible

[1] Author to whom correspondence should be addressed. Electronic mail: meyerfw@ornl.gov

approach is to use metallic ion implantation. The electrode surface resistivity must be in the range $10^3\ \Omega < R_s < 10^8\ \Omega$ and the implant must be sufficiently robust to survive repeated cycling between room temperature and an operating temperature of 0.3 K. Furthermore, since the electrodes will be subject to large neutron fluences, the implanted species must have low activation to minimize resulting gamma radiation that would reduce experimental sensitivity. To prevent distortions that would interfere with strict magnetic-field-uniformity requirements (less than 3 ppm/cm), the electrodes must also be non-magnetic. This paper reports the status of ion-implantation R&D efforts to produce sample electrodes that can meet all the above requirements, using a newly developed and implemented beam-rastering and profile-measurement system. Initial results are presented for PMMA implantation by tungsten ions with focus on characterizing the induced changes of PMMA surface properties as a function of the ion implantation energy and fluence.

The modification of material properties of polymers by implantation of metal ions has been investigated for many years. Sofield *et al*. [Sofield, 1992] studied the formation of a carbonaceous layer in polyether ether ketone (PEEK) by implantation of various ions. They found that the conductivity of this carbonaceous layer depends on the ion energy deposition rate. Specifically, for energy deposition rates above 30 MeV mg^{-1} cm^{-2}, the layer is in the form of a more-conductive damaged graphite structure, whereas for lower rates, a less-conductive diamond-like carbon structure forms. Niklaus and Shea [Niklaus, 2011] investigated implantation of gold and titanium ions in polydimethylsiloxane (PDMS) for fluences up to 5 x 10^{16} cm^{-2} for 2.5-10 keV ions. They described their results using percolation theory and found different behaviors for the two implanted species. Due to its higher electronegativity (2.5 vs. 1.54 eV for Ti), gold tends to form crystalline nanoparticles and exhibited Ohmic conduction between the metallic clusters, whereas the Ti-implanted polymer acts more as a doped elastomer with conduction due to shifted Fermi levels. Of more direct application to this present investigation are the results of Bazarov *et al*. [Bazarov, 1995], who implanted PMMA with 40-keV ions of Fe, Ag, and Pb. Transmission electron microscopy (TEM) measurements revealed that the implantation process produces granular films of the metals just below the polymer surface, consisting of metallic particles of widely varying sizes [Petukhov, 2001]. Conduction in this material is due to both the carbonaceous layer and the granular metal film. Two mechanisms have been identified for conduction in the granular metal film via intergrain electron transport: (1) direct electron tunneling between the grains [Adkins, 1982], which becomes dominant at very low temperatures, and (2) thermally-activated "hopping" [Sheng, 1983]. Bazarov *et al*. found that for a broad distribution of metallic grain sizes in the PMMA, the surface resistivity R varied with the temperature as $\ln R \sim T^{-1/2}$.

In the present article, we first describe our experimental approach for producing the metallic ions at the desired implantation energy and for characterizing the spatial distribution of such ion beams. We then describe our set-up for exposing the target PMMA samples to a large fluence of tungsten ions in both a fixed and a rastered configuration; the rastered configuration is needed to produce, using small-size ion beams with Gaussian-like profiles, the sufficiently large uniform areas of enhanced surface

conductivity on the PMMA substrate required for subsequent high-voltage compliance tests. Finally, we will describe analysis of the composition of these sample electrodes by x-ray photoelectron spectroscopy (XPS) and initial measurements of surface resistivity changes. . Tungsten was used for the present measurements only as a prototypical metallic specie with a reasonable electronegativity (2.36 eV) that had been recently developed in our facility for an unrelated experiment [Meyer, 2013] to test our overall experimental approach and thus does not necessarily represent the final choice of metallic specie meeting all the required properties enumerated above.

II. EXPERIMENTAL METHOD

A. Ion Beam Production

Multicharged tungsten ions are produced by a Caprice electron-cyclotron-resonance (ECR) ion source at the ORNL Multicharged Ion Research Facility [Meyer, 2001] using the Metal Ions from Volatile Compound (MIVOC) technique [Koivisto, 1998] based on tungsten hexacarbonyl vapor as the source gas. The ions are extracted from the source at 6.5-kV to 12-kV acceleration potentials and then individual charge states are selected with an analyzing magnet. A typical W charge state distribution of beams extracted from the ECR ion source is shown in Figure 1. Note that due to the large Faraday cup aperture, the resolution is not sufficient to separate the four naturally occurring isotopes of tungsten; each charge-state peak in the figure is instead a superposition of the individual isotopes, each slightly shifted in analyzing field due to the slight differences in mass. The selected W^{4+} ion beams used in the present study are then focused onto the PMMA targets using a large-acceptance beam-deceleration lens immediately upstream of the target, as previously described [Hijazi, 2013]. With no deceleration and 12 kV source potential, the tungsten ions reach the PMMA surface with energies of 48 keV; by floating the samples at 11 kV, and optimizing the ion optics of the upstream decel module, intense beams could be obtained also at 4 keV impact energy. Typical W^{4+} ion currents delivered to the PMMA targets were 2.0 μA for 48-keV ions and 0.7 μA for 4-keV ions. A similar method was employed to produce the 60-keV Ti^{5+} and 50-keV Ar^{5+} ions employed in the preliminary implantation studes, using source gases of (trimethyl)pentamethyl-cyclopentadienyl titanium and argon, respectively.

B. Ion Beam Characterization

In order to properly characterize the properties of the metal-ion-implanted samples as a function of the ion fluence incident on the PMMA targets, the spatial characteristics of the ion beams used for implantation must first be determined. To this end, an apparatus was developed to permit accurate measurements of the 2D profile of the ion beams at the plane of the PMMA targets. The photo in Figure 2 shows the part of this device inserted into the beam line after the deceleration module; the upper portion is the holder for the PMMA targets, the lower portion is the ion-beam-profile monitor. The beam-profile monitor consists of a well-shielded and suppressed Faraday cup located behind a tantalum shield with a 1-mm square aperture. The target holder includes an exposed area

above the mounted sample on which the incident ion beam current can be measured. Immediately above this open area a biasable electron filament is mounted which is energized at 6V, 1.7A during PMMA irradiation to mitigate sample charging. The target holder and beam profile monitor assembly are mounted on a three-axes motion assembly driven by a stepper-motor system. VisualBasic-based software was developed to scan the beam profile monitor in user-specified steps over a 2D surface in the plane of the PMMA target, and to collect the ion current on the Faraday cup through the 1-mm^2 aperture as measured with an electrometer with an accuracy of 2% or better. The total suppressed current to the tantalum shield in front of the Faraday cup could be simultaneously measured to permit normalization of the profile in cases where the total ion-beam current varies during the profile measurement which typically required several minutes to complete. The measured ion profiles are integrated numerically to determine the total beam current or flux at the plane of the target. Typical W^{4+} ion profiles measured by this method are shown in Figure 3 for 48-keV and 4-keV implantation energies, with total currents of 1.9 μA and 0.6 μA, respectively. The vertical distributions in each case are narrow, with a FWHM of about 1.5 mm. The distributions in the horizontal mass/momentum dispersion plane, on the other hand, are significantly broader, primarily due to the dispersion by the upstream analyzing magnet of the 4 stable isotopes of tungsten in the 182-186 amu mass range with natural abundances between 14.4 and 30.6%.

C. Implantation in PMMA

Implantation of tungsten ions into the PMMA targets was investigated in a fixed as well as a rastered configuration. In parallel with the development of the target rastering system, initial implantation studies were performed with fixed PMMA targets of two sizes (8 mm x 16 mm x 0.5 mm and 16 mm x 16 mm x 0.5 mm) to gain insight into the dependence of surface resistivity on ion-beam energy and fluence. In this configuration, the implanting ions were focused onto a single spot on each PMMA target. During implantation, the targets were flooded with low-energy electrons (energy about 30 eV, typical target holder current 50 μA) to prevent charging of the PMMA surface. The spatial distributions of the implanted fluences in these cases corresponded to the spatial distribution of ions in the incident beam as shown in Figure 3. Analyses of these fixed-target exposures will be given in Section III.

In order to implant tungsten ions over a larger PMMA area, necessary for follow-on high-voltage compliance tests, additional VisualBasic-based software was developed to permit rastering the incident ion beam over a user-specified area of the PMMA sample under PC control. The PMMA targets for these studies measured 28.6 mm x 28.6 mm x 4 mm. Initial characterization of the 2D ion-flux profile using the technique described in the previous section always preceded the large-area rastering exposure. Next, under PC control, the target holder is positioned to intercept the incident beam on the open area just above the PMMA sample to monitor the incident beam current, I_i. After positioning the target holder to one corner of the PMMA sample area to be exposed, the holder is translated continuously at a rate of 1 mm/s in the vertical (y) direction until the ion beam center reaches the opposite edge of the selected target area. The target is then shifted

0.25 mm in the horizontal (x) direction, and the vertical movement reverses to move the target back across the ion beam to the starting y position. This process is repeated until the entire selected area of the PMMA sample has been exposed. The horizontal step size (0.25 mm) was chosen much smaller than the ion beam dimensions to ensure a uniform exposure during rastering. For the 48-keV implantation, the raster area was 10 mm wide (x-direction) by 30 mm high (y-direction); for the 4-keV implantation the raster area was 5 mm wide by 30 mm high. The 30 mm movement range in the y-direction was chosen to expose the target from one edge to the opposite edge in that dimension to simulate large-area electrode production and to facilitate surface-resistivity-change measurements at cryogenic temperatures. Once the entire selected target raster area has been exposed to the ion beam, the target is returned to the beam current monitoring position, the electron flood filament is turned off, and the ion current remeasured and recorded. This cycle of target rastering and current monitoring was repeated until the desired ion fluence on the target has been reached; each cycle for the 48-keV implantation required approximately 20 minutes, and about half that time for the 4-keV implantation. The smaller raster area was selected for the 4 keV implant in order to keep the total irradiation time required for the desired fluence at a reasonable level.

From the total exposure time T_{tot}, the average measured ion current, I^{ave}_{i}, and the raster area A, one can determine an average fluence on the target for a given exposure by $I^{ave}_{i}T_{tot}/A$. To study the spatial distribution of the fluence resulting from a given ion flux distribution, numerical simulations of the raster process were performed. Simulated rastered fluence distributions for the measured 48-keV and 4-keV ion flux distributions (shown in Figure 3) are presented in Figure 4. Consistent with standard convolution considerations, the simulations of the raster process indicate uniform fluence areas of height and width roughly equal to the raster height or width minus the FWHM of the ion beam in the two respective directions, with edge region widths comparable to the ion beam widths in the respective planes. At both investigated energies, the peak fluences in the central plateau of the simulated distributions are about 30% higher than the average fluence on the targets as calculated above.

D. Surface Composition and Resistance Measurements

X-ray induced photoelectron spectroscopy (XPS) is a surface-sensitive analytical technique providing specific information on elemental and chemical surface composition. The Thermo Scientific K-Alpha XPS instrument used for the present measurements features 30-micron spatial resolution (variable from 30 to 400 microns), precise stage movement allowing elemental and chemical mapping over large areas, and an *in-situ* Ar^+ ion gun for sputter cleaning and depth profiling measurements. Advanced software features allow principal component analysis of map data and the ability to retrospectively determine spectral information from map data.

The depth profiles were determined by XPS measurements performed during sputtering with a 3-keV Ar ion beam. The sputter-beam surface-removal rate, calibrated for SiO_2, was estimated for PMMA by using the simulation code SRIM [Ziegler, 1985] to determine the ratio of sputtering yields for 3-keV Ar ions at normal incidence on SiO_2

and PMMA targets. The thus deduced PMMA sputter removal rate was assumed to be unaffected by metal ion implantation, or by ion-impact-induced modifications of the PMMA polymer [Zekonyte, 2005].

Surface resistivity changes of the W-implanted PMMA targets exposed in the fixed configuration were measured using a two point contact method, with the probe consisting of two contacts of fixed 3-mm separation pressed manually into the irradiated surface. For measurements on the large-area rastered targets, the probe consisted of copper clamps with an Indium gasket between the clamps and the conductive surface in order to ensure a well-defined surface-contact area independent of temperature. Resistances were measured using a Fluke Model 77IV digital multimeter. For both probe geometries, the surface resistances of virgin (unexposed) PMMA surfaces were beyond the measurement capability of our multimeter ($> 10^{10}\ \Omega$). Since surface resistance and resistivity are measured in the same units, and are related by a constant factor depending only on probe geometry, measured changes in surface resistance as function of implantation conditions or sample temperature, using either probe geometry, are expected to reflect corresponding changes in the relevant intrinsic surface resistivities. With this in mind, the terms surface resistance, surface resistivity, and surface conductivity (i.e., the reciprocal of surface resistivity) are used interchangeably throughout.

III. RESULTS

A. Preliminary Test Exposures

Preliminary implantation exposures were carried out with keV-energy-range Ti and Ar ion beams to guide fluence choices for the subsequent W ion exposures, as well as to investigate possible target graphitization effects which might mask surface-conductivity enhancement due to metal ion implantation. Regarding the first issue, implantation with 60-keV Ti^{5+} ions to fluences of $2\text{-}4\times10^{15}cm^{-2}$ showed no measurable surface conductivity. To address the issue of target graphitization, we exposed the PMMA test coupon to a 50-keV Ar^{5+} ion fluence similar in magnitude to the Ti beam exposure, and again found no enhanced surface conductivity. XPS analysis of both Ti and Ar beam spots, both of which were clearly discernible to the unaided eye, indicated significant changes in the C(1s) and O(1s) lineshapes in comparison to an unexposed PMMA test coupon, as illustrated in Figure 5 for the Ar-exposed spot. The loss of "PMMA-like peaks" in the C(1s) and O(1s) core level spectra, together with the overall attenuation of the O(1s) peak height, indicate that both ion beams evidently act to disrupt the chemical structure of the virgin PMMA surface. During depth profiling XPS measurements of a virgin PMMA sample using 3-keV Ar ions, a similar change in C(1s) and O(1s) lineshapes and relative peak heights was observed. While such ion-beam-induced disruption of polymer surfaces is well known and documented for PMMA and many other polymer systems [Zekonyte, 2005], for the present ion beams and fluences, these changes in spectral features resulted in no measureable changes in surface resistivity for either the 50 keV-energy Ti and Ar ion-beam test exposures, or the low-energy Ar sputter-beam exposed PMMA coupon.

B. Stationary Targets

Following these preliminary test exposures with Ti and Ar beams, we switched to W beams because of their higher electronegativity (2.36 eV) , and sought to establish the W fluence levels required to obtain measurable surface conductivity for this metal specie. Based on the results of our preliminary Ti beam test exposures, only W ion fluences in excess of $10^{16}cm^{-2}$ were investigated. Searching for correlations between surface conductivity changes and near-surface metal-concentrations, we performed XPS analyses on the W-ion-implanted PMMA targets exposed in a stationary configuration. A representative measured XPS spectrum is given in Figure 6(a), showing peaks associated with W, C, and O photoelectrons after exposure to a 7.0 x 10^{16} cm^{-2} fluence of 48-keV W^{4+} ions. As shown in Figure 6(b), higher resolution core-level spectra in the W(4f) region are able to distinguish implanted tungsten in metallic W(m) and oxide W(o) forms. Figure 7 shows XPS results for 8 mm x 16 mm PMMA samples irradiated by 48-keV W ions to fluences of 1.75 x 10^{16} cm^{-2}, 3.5 x 10^{16} cm^{-2}, and 7.0 x 10^{16} cm^{-2}, obtained using the mapping feature of the XPS instrument together with chemical phase analysis software. In each case, the area of the PMMA exposed to the ion beam and analyzed with XPS was clearly discernible to the unaided eye. The different colors represent regions of the target with different "phases" or surface compositions as identified in the accompanying bar graphs. As seen from the figure, the resulting metallic W near-surface atomic concentrations were found to be in the 10-15% range, and to increase with increasing fluence. Interestingly, at the highest of the three fluences, two distinct phases are identified in the beam-exposed region having different ratios of W in metallic versus oxide forms. The crosses in each phase map indicate the location of XPS depth-profile measurements performed for each fluence.

The respective depth profiles of the implanted W atoms are shown in Figure 8. For the two lowest fluences, the W depth profiles (dashed and dash-dot curves) are very similar, with the W atom percentages peaking at about 23-24% just below the surface and quickly drop to less than 5% by a depth of 15 nm. The higher peak W concentrations indicated in Figure 8 compared to those indicted in Figure 7 result from the removal of surface contaminants, particularly oxygen, during the initial phases of the Ar sputtering process. Interestingly, the depth profile for the highest fluence exposure (solid curve), is markedly different, having a significantly broader peak at about 29% that extends deeper than 5 nm but then decreases more steeply with depth than the lower fluence profiles. At a depth of 15 nm, the W-atom percentage is still around 10% for the high fluence exposure. It is possible that this depth-profile change is due to a sample-temperature increase from proximity to the hot electron flooding filament whose heating effect increases with increasing exposure times, since some surface melting was observed on the sample edge closest to the filament (in the subsequent rastering exposures, the filament was located farther away from the samples and edge melting was no longer observed). Alternatively, it is possible the characteristics of the near-surface PMMA layers are sufficiently changed at the higher fluences due to the presence of implanted W and/or the ion-induced disruption of polymer structure already noted in connection with Figure 5 to alter the shape of the implantation depth profile.

To see how the W near-surface atomic concentrations correlated with surface conductivity, the surface resistivities of these three targets were then measured at room temperature using a two-point contact method. The positions of the measurements were chosen on the basis of features discernible to the eye visible on the exposed targets which corresponded closely to the XPS maps of Fig. 7. The measurements were carried out with the probe oriented along the long dimensions of the visible fingers. No measurable conductivity was found for the target with the lowest fluence. For the target exposed to a fluence of 3.5 x 10^{16} cm^{-2}, surface resistances in the range of 1.7-10 GΩ were measured in regions of highest W atom concentrations indicated in Fig. 7(b). Finally, surface resistances of 7-30 MΩ were measured for the target exposed to the 7.0 x 10^{16} cm^{-2} fluence. On the basis of these measurements using stationary-target beam exposures, the minimum fluences required for the rastered-target exposures described in the next section were thus identified.

In order to obtain an indication of the relative importance of near-surface W concentrations and the total implanted W dose or fluence, we also explored the energy dependence of W-ion implantation. To this end, additional exposures were carried out at W-impact energies of 13 and 180 keV, both to fluences of ~ 5×10^{16} cm^{-2}. Surface-resistance measurements were carried out for both exposed PMMA samples, and showed lowest values of 10-18 MΩ, i.e., in the same range as the above 48-keV W ion exposures.

C. Rastered Targets

With the fixed-configuration beam-exposure results as a guide, large-area exposures were carried out next. Figure 9 shows XPS maps of the W-atom surface concentration of PMMA after exposure to a 48-keV W^{4+} ion fluence of 5.9 x 10^{16} cm^{-2} (average) over a 30 mm x 10 mm raster area. The XPS analysis was focused on the central portion of the target that would be used in conductivity measurements. The 2-D plot in (a) represents the central portion of the raster area and exhibits a very uniform W-atom concentration with the exception of a defect near the middle due to inadvertent surface damage during removal from the implantation chamber. One-dimensional profiles of the W-atom surface composition along vertical cuts through the analysis region (marked by arrows in Fig. 8(a)) are shown in Fig. 8(b). The W-atom percentage is very uniform in the vertical (y) direction, with values in the 22-24% range, except for cuts 3-5 that intersect the damaged spot.

At room temperature, T_0 = 300 K, the sample surface resistivity R_0 measured 1 MΩ. After submersion in liquid nitrogen (77 K), its surface resistivity increased to 10.4 MΩ. After the sample was warmed back up to room temperature, the surface resistivity returned to a value of 1.6 MΩ. This observed temperature dependence is consistent with that of the surface resistivity measurements of Ag-ion-implanted PMMA by Bazarov *et al.* [Bazarov, 1995], that is, $R = R_0\, exp[(T_0/T)^{1/2}]$. Measurements were not extended to lower temperatures to see if a transition to a weaker temperature dependence occurred as observed by Bazarov et al.

In order to extend our fixed target configuration results to lower energies which overlap with impact-energy capabilities of existing large-area Plasma Immersion Ion Implantation (PIII) facilities [Wei, 2005], we also performed a 4-keV W ion implantation. XPS measurements of the W surface concentration of a PMMA target exposed to an average fluence of 6.2 x 10^{16} cm^{-2} of 4-keV W^{4+} ions rastered over a target area of 30 mm x 5 mm are shown in Figure 10, which indicate the beam-exposed area in red. Transverse scans of tungsten atom concentrations were determined along three horizontal lines cutting across the analysis area at positions indicated in Fig. 10(a). The obtained W-atom percentage profiles, shown in Fig. 10(b), exhibit a broad flat plateau about 8 mm wide with atom percentages in the 24-27% range.

For comparison, Fig. 10(b) also shows the fluence profile predicted by the rastering simulation described previously for the measured ion beam profile of Fig. 3(b). Interestingly, the predicted fluence profile is narrower and significantly less flat topped than the measured W-concentration profile. A similar width difference between fluence and W-concentration profiles was observed for the 48-keV tungsten beam exposure (rastered target). This suggests the possibility that the near-surface W concentration saturates at some level, and that with additional fluence the concentration penetrates to greater depths instead, similar to the trend suggested in Figure 8. Certainly, when the near-surface composition becomes 20-30% W, the possibility of W impact on already-implanted W atoms becomes significant, which could increase the mean implantation depth. These speculations are confirmed by comparisons of XPS depth profile measurements performed in the maximum fluence region in the center of the raster area and at the edge half-fluence point, as shown in Figure 11, which indeed show a deeper W depth profile in the center of the raster area. Figure 12 shows a similar difference in depth profiles between full- and half-fluence points for the rastered 4-keV W implant. The surface resistance measured on this target was about two orders of magnitude higher immediately upon removal from the implantation chamber than was measured for the 48-keV W exposed PMMA target. A repeat measurement the following day indicated a surface resistance beyond the range that could be measured with our multimeter. In view of the similar W ion fluence to which this sample was exposed, the very high surface resistance seen for the 4-keV W ion exposure is surprising, especially when recalling that regions of measurable conductivity were found for the fixed target exposure with a fluence of only 3.5 x 10^{16} cm^{-2}, well below the average fluence for the 4-keV W implantation, and that measurable conductivities were found for the 13- and 180-keV tungsten implants. One clue to the conductivity difference may be found in Figures 11 and 12, which show, in addition to total W concentrations, depth profiles of the metal and oxide W forms. Comparison of the two figures shows that, irrespective of the local fluences, the high-energy implant resulted in predominantly metallic W throughout the entire depth profile, while the lower-energy implant resulted in an implanted W metal-to-oxide ratio closer to 1. XPS observation of a high-metallic-W abundance suggests prefential W bonding with other W atoms to form clusters, which enhances surface conductivity. On the other hand, XPS observation of a significant W oxide component suggests that the implanted W atoms bond primarily to the polymer matrix, which most likely has only a minor effect on surface conductivity.Our results therefore suggest that W cluster formation in PMMA is implantation-energy dependent, with clusters being

formed at 48 keV (leading to enhanced surface conductivity), and predominant matrix bonding occurring at 4 keV (with no conductivity enhancement).

IV. CONCLUSIONS

As an initial attempt to show proof-of-principle of one method for preparation of electrodes suitable for use in the nEDM experiment, PMMA targets have been implanted with 4-180 keV tungsten ions in fixed and/or rastered configurations, the latter to produce sufficiently conductive and uniform surfaces over areas larger than the implanting ion beam for follow-on HV compliance tests and cryogenic-resistance measurements. For the fixed target exposures, surface composition and resistance were investigated as a function of fluence of 48-keV ions, with fluences ranging from 1.75 to 7.0 x 10^{16} cm^{-2}, and, for fixed fluence, at energies ranging from 13-180 keV. For fluences of 3.5 x 10^{16} cm^{-2} or more, measurable conductivities falling within the range acceptable for the nEDM experiment were found at energies ranging from 13-180 keV. Surface composition and resistance were also studied for a PMMA target implanted to an average fluence of 5.9 x 10^{16} cm^{-2} by 48-keV W^{4+} ions rastered over a 30 mm high x 10 mm wide area. The measured resistance for this target followed the temperature dependence reported by Bazarov *et al*. [Bazarov, 1995] for temperatures down to 77 K. As determined by XPS, the surface composition of this 48-keV ion-implanted target was very uniform over a sufficiently large area suitable for follow-on high-voltage compliance tests. For a PMMA target exposed to a 6.2 x 10^{16} cm^{-2} fluence of rastered 4-keV W^{4+} ions, however, no stable measurable surface resitivity was found, despite the fairly uniform surface compositions of up to about 30% W atoms determined by XPS in the rastered area. For both implantation energies investigated in the rastered configuration, XPS measurements showed that the W surface concentration profiles are systematically broader and more flat-topped than the corresponding simulated-fluence profiles. Tungsten-atom-depth profile measurements revealed systematic widening of the implanted W depth profiles at higher fluences, suggesting that, despite the flat-topped W surface concentrations, the total volume W concentration profiles do in fact follow the W beam fluence profiles. Deconvolution of the W XPS peaks to distinguish the metallic and oxide forms further showed that for the 48-keV implant, the implanted W is predominantly in metallic form, whereas for the 4-keV implant, the oxide form is of equal or greater prominence, especially in the near surface region, which may explain the observed differences in surface conductivities at the two energies. To explore possible scenarios that might lead to different implanted W chemical forms at the two energies, TEM measurements are planned to assess whether clustering of the implanted tungsten atoms is occurring at both energies, since clustering versus matrix bonding of the W is very likely to affect the implanted W metal to oxide ratios.

ACKNOWLEDGEMENTS

This research was sponsored by the LDRD Program of Oak Ridge National Laboratory, managed by UT-Battelle, LLC, for the U.S. Department of Energy. HH was appointed through the ORNL Postdoctoral Research Associates Program administered jointly by Oak Ridge Institute of Science and Education (ORISE), Oak Ridge Associated Universities (ORAU) and Oak Ridge National Laboratory (ORNL). XPS instrument supported by Oak Ridge National Laboratory's Shared Research Equipment (ShaRE) User Program, which is sponsored by the Office of Basic Energy Sciences, U.S. Department of Energy.

REFERENCES

[Adkins, 1982] C.J. Adkins (1982), "Microscopic aspects of conduction in discontinuous metal systems,"J. Phys. C. Solid State Phys.,15, 7143.

[Bazarov, 1995] V.V. Bazarov, V.Yu. Petukhov, V.A. Zhikharev and I.B. Khaibullin (1995)"Conductivity of the Granular Metal Films Obtained by High Dose Ion Implantation into PMMA," MRS Proceedings, 388, 417.

[Golub, 1994] R. Golub and S.K. Lamoreaux (1994), "Neutron electric-dipole moment, ultracold neutrons and polarized ^{3}He," Phys. Reports, 237, 1.

[Hijazi, 2013] H. Hijazi, and F.W. Meyer (2013), "A large-acceptance beam-deceleration module for retrofitting into ion-source beam lines," Rev. Sci Instrum., 84, 033305.

[Koivisto, 1998] H. Koivisto, J. Arje, and M. Nurmia (1998), Metal ions from the volatile compounds method for the production of metal ion beams," Rev. Sci. Instrum., 69, 785.

[Meyer, 2001] F.W. Meyer (2001), "ECR-based atomic collision physics research at ORNL MIRF," in *Trapping Highly Charged Ions: Fundamentals and Applications*, edited by J. Gillaspy (Nova Science Publishers, Huntington, NY), p. 117.

[Meyer, 2013] F. W. Meyer, H. Hijazi, M. E. Bannister, P. S. Krstic, J. Dadras, H. M. Meyer III, C. M. Parish, "He-ion and self-atom induced damage and surface-morphology changes of a hot W target," to be published, Physica Scripta (2013).

[Niklaus, 2011] M. Niklaus and H.R. Shea (2011),"Electrical conductivity and Young's modulus of flexible nanocomposites made by metal-ion implantation of polydimethylsiloxane: The relationship between nanostructure and macroscopic properties," Acta Materialia, 59, 830.

[Petukhov, 2001] V.Yu. Petukhov, M.I. Ibragimova, N.R. Khabibullina, S.V. Shulyndin, Yu.N. Osin, E.P. Zheglov, T.A. Vakhonina, and I.B. Khaibullin (2001),"The influence of the polymer matrix structure on the ion beam synthesis of metal-polymer thin films," Polymer Sci. Ser. A, 43, 1154.

[Sheng, 1983] P. Sheng and J. Klafter (1983), “Hopping conductivity in granular disordered systems,” Phys. Rev. B, 27, 2583.

[Sofield, 1992] .J. Sofield, S. Sugden, C.J. Bedell, P.R. Graves, and L.B. Bridwell (1992), “Ion beam modifications of polymers,” Nucl. Instrum. Methods Phys. Res.B, 67, 432.

[Wei, 2005] R. Wei, T. Booker, C. Rincon, and J. Arps (2005), “Metal plasma immersion ion implantation and deposition (MPIII and D) using a metal plasma electron evaporation source (MPEES),” Surface Coatings Tech., 200, 579.

[Zekonyte, 2005] J. Zekonyte, V. Zaporojtchecko, and F. Faupel (2005), “Investigation of the drastic change in the sputter rate of polymers at low ion fluence,” Nucl. Instrum. Methods Phys. Res. B, 236, 241.

[Ziegler, 1985] J.F. Ziegler, J.P. Biersack and U. Littmark (1985), SRIM (Stopping and Range of Ions in Matter), "The Stopping and Range of Ions in Solids," Pergamon Press, New York.

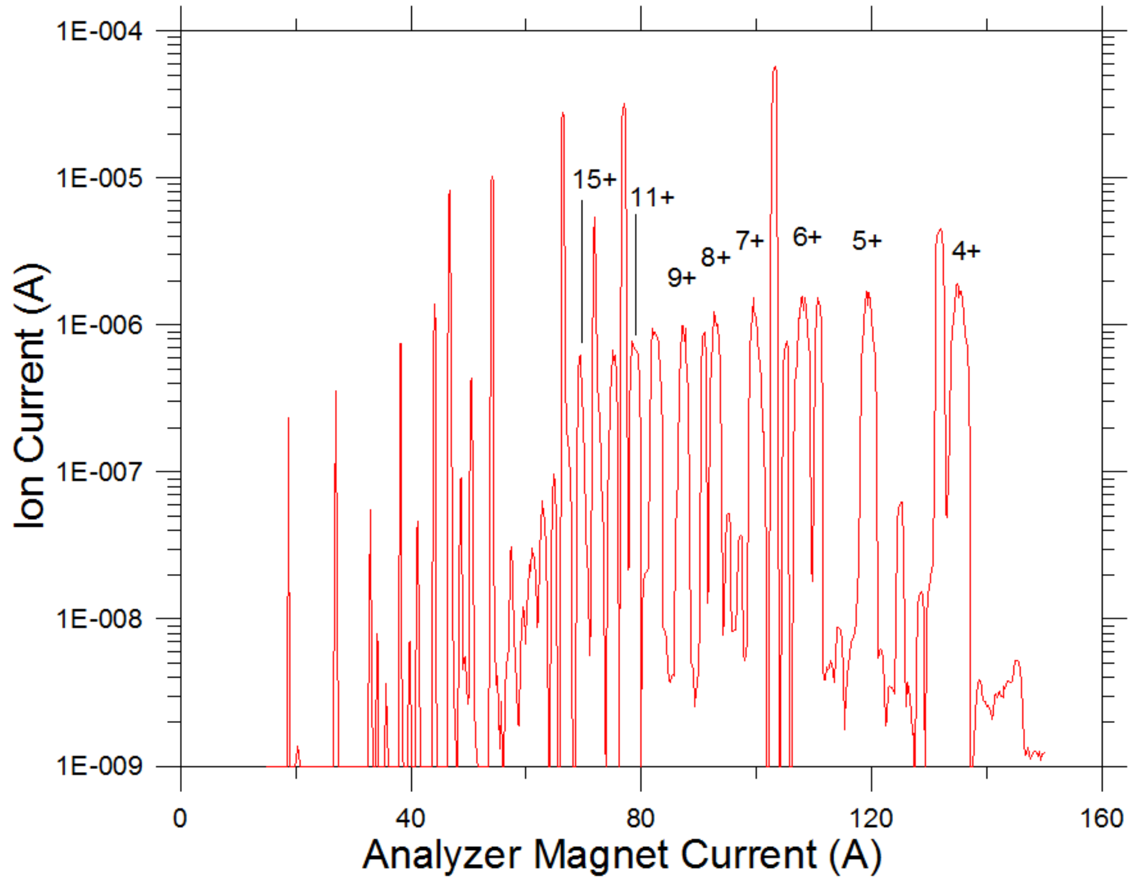

Figure 1. Charge state distribution of tungsten ions extracted at 12 kV from the ORNL Caprice ECR ion source, with selected charge states of tungsten ions identified above the corresponding peaks.

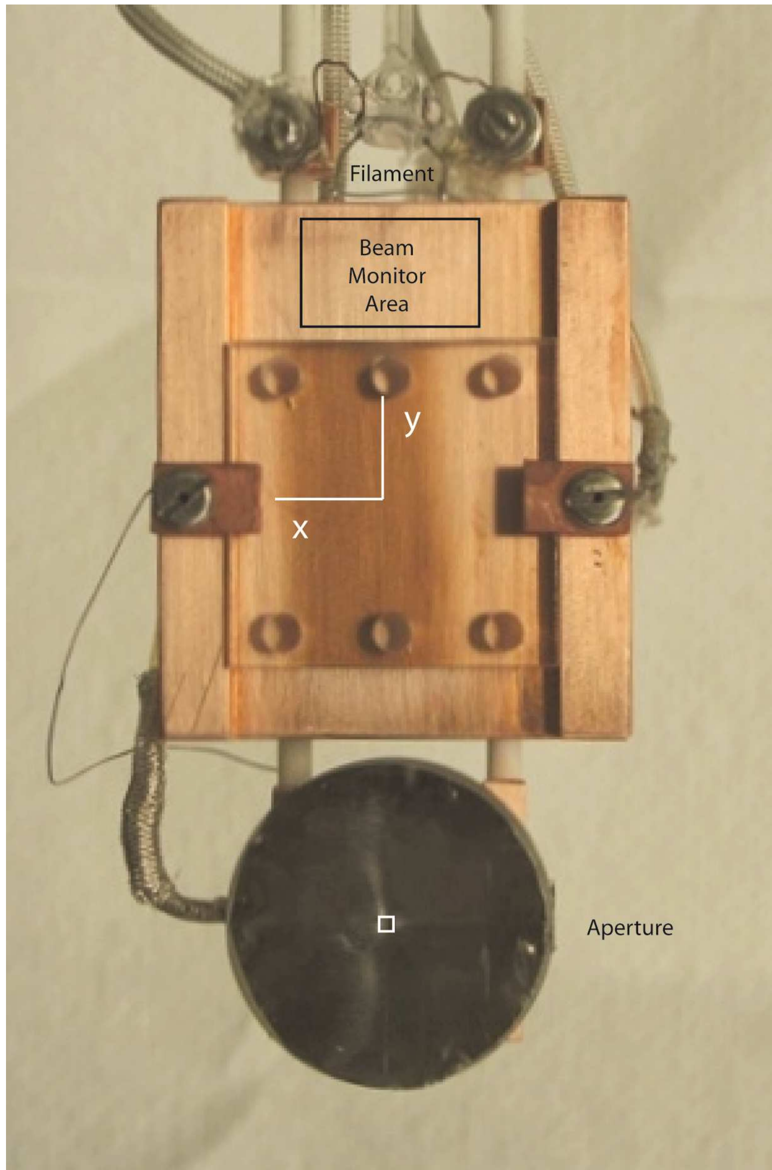

Figure 2. PMMA target holder (top) and beam profile monitor (bottom, note 1x1 mm aperture through which beam is measured) positioned in the beam line of the ORNL Caprice ECR ion source and manipulated with a three-axes stepper motor system. The PMMA target shown in this photo has been exposed to 48-keV W^{4+} ions and rastered over a 30 mm x 10 mm area. The filament floods the target with low-energy electrons to prevent charging of the PMMA surface The area at the top of the target holder above the PMMA target is used for monitoring ion beam current during rastered exposures (see text).

(a)

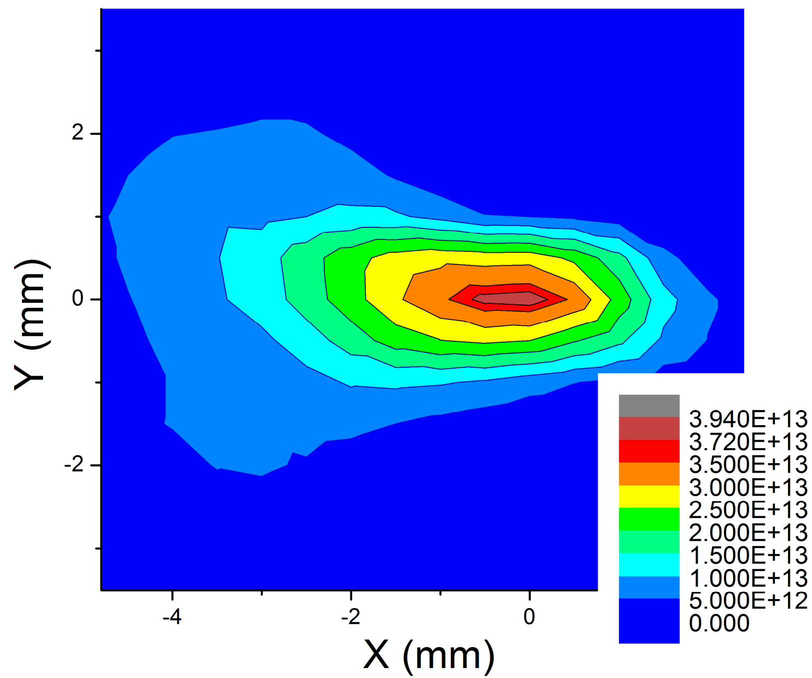

(b)

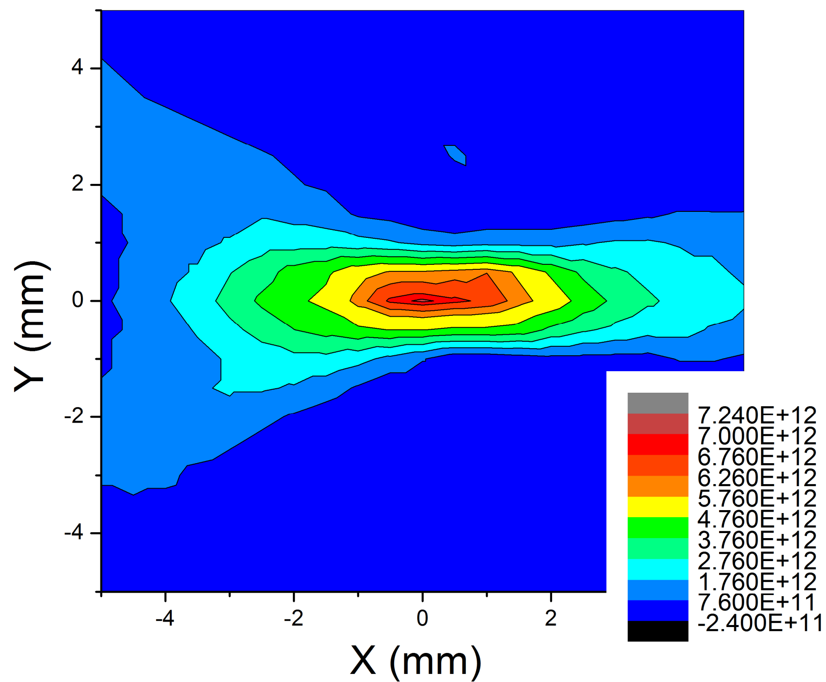

Figure 3. (a) Ion beam flux (ions/cm^{2}s) profile for 48-keV W^{4+} measured at the plane of the PMMA target. (b) Ion beam flux profile for 4-keV W^{4+}. Both profiles were measured using the beam profile monitor Faraday cup with 1x1 mm entrance aperture and the 2-D raster set-up described in the text.

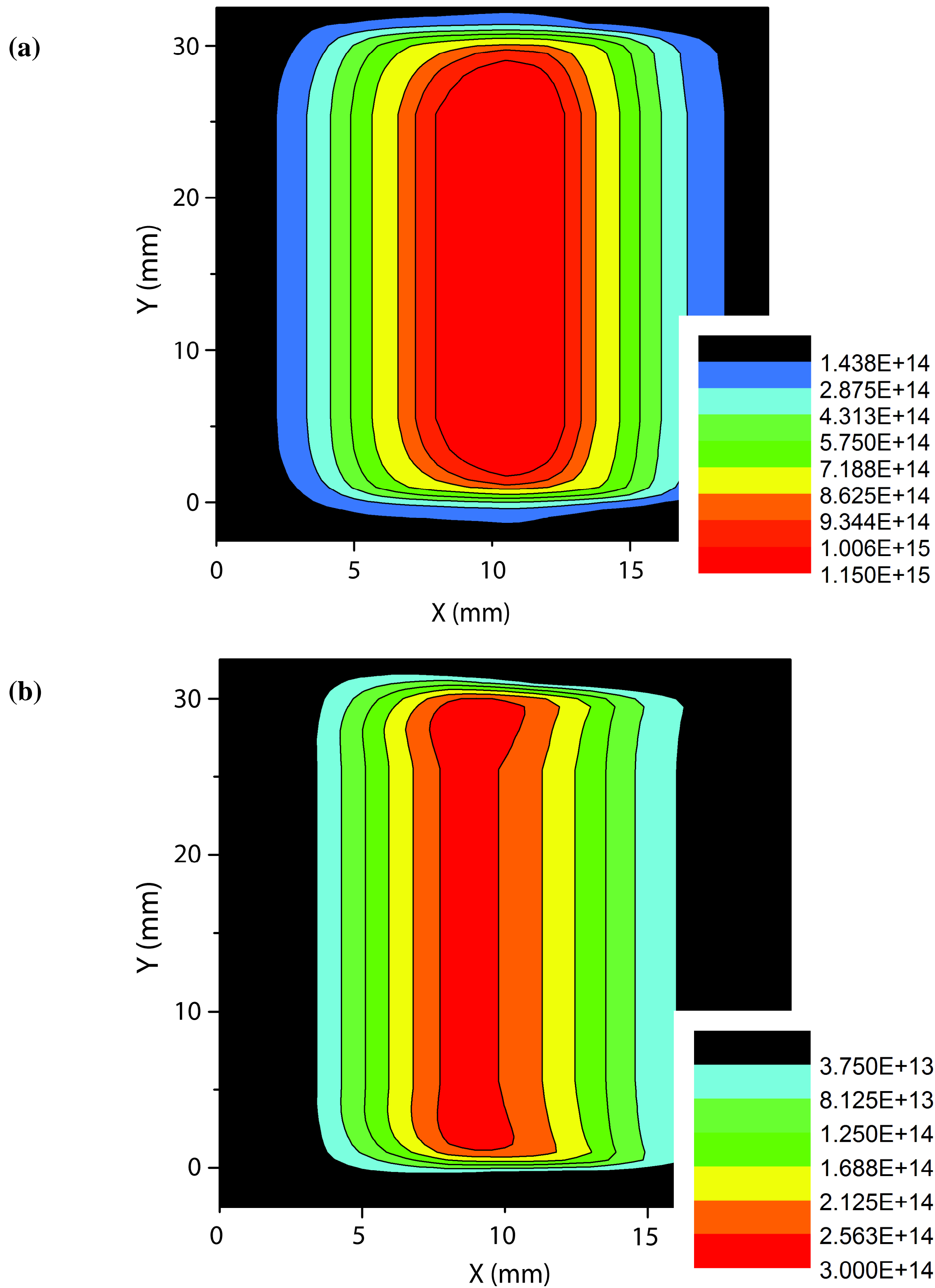

Figure 4. Simulated fluence distributions for a single-cycle raster of a PMMA target using the measured W^{4+} ion beam profiles of Figure 3. (a) 48-keV ions with total incident beam current of 1.9 μA; target rastered over 30 mm high x 10 mm wide area. (b) 4-keV ions with total incident decelerated beam current of 0.6 μA; target rastered over 30 mm high x 5 mm wide area.

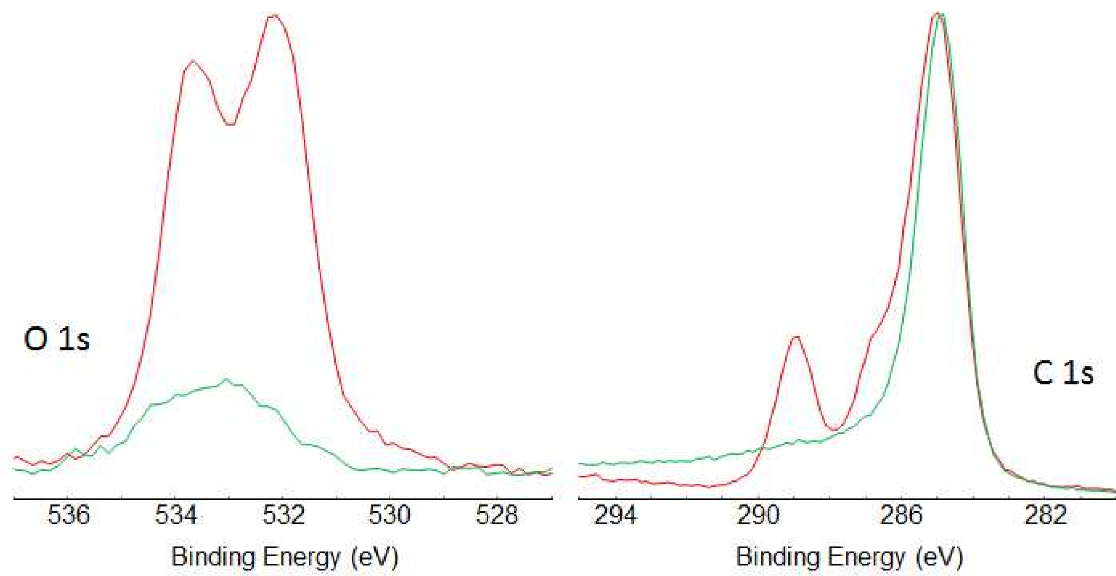

Figure 5. XPS C(1s) and O(1s) lineshape comparisons of virgin PMMA (upper red curves) and ion-beam exposed PMMA (lower green curves), showing ion-impact-induced disruption of PMMA polymer structure after exposure to a 4 x 10^{15} cm^{-2} fluence of 50 keV Ar^{5+} ions. At the investigated impact energies, these disruptions had no measurable effect on surface conductivity.

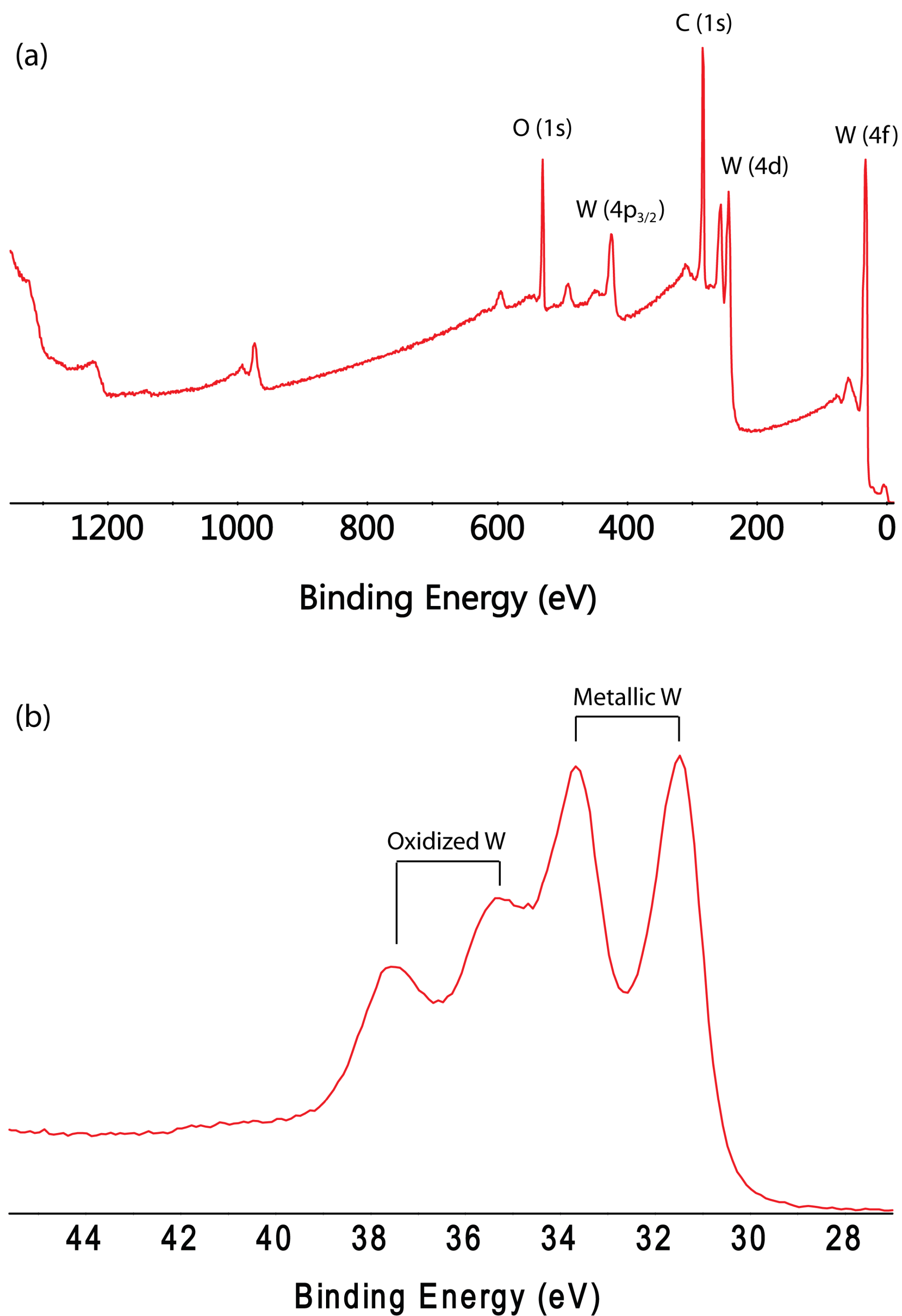

Figure 6. (a) X-ray Photoelectron Spectrum (XPS) for PMMA exposed to 48-keV W^{4+} ions in a fixed configuration. (b) High-resolution core-level XPS W spectrum indicating presence of both metallic and oxidized implanted W for this implantation condition. This typical spectrum is for a single position within the exposed area.

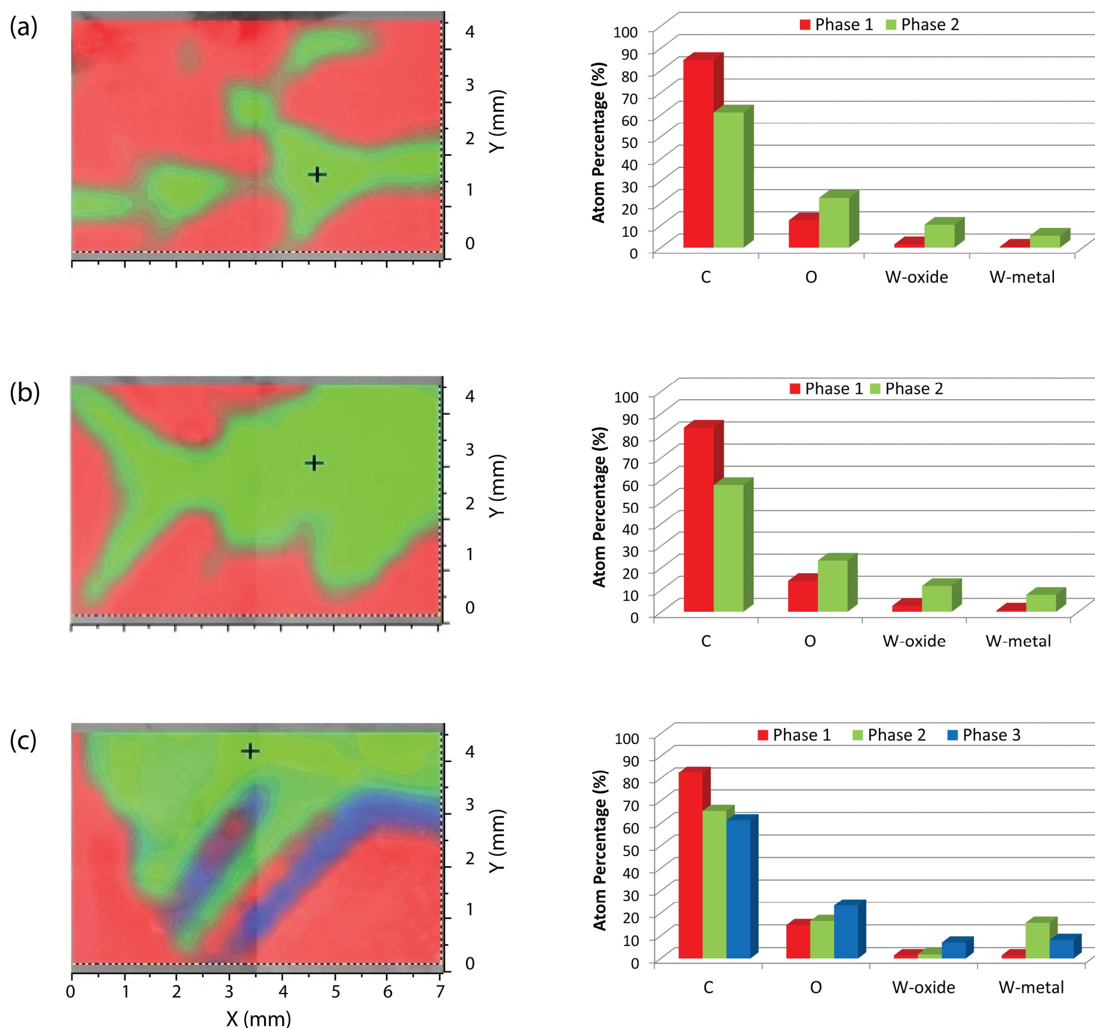

Figure 7. Surface compositions of PMMA targets exposed to 48-keV W^{4+} ions in the fixed configuration as measured by the XPS technique. The different colors represent regions of different atom percentages for the C, O, and W constituents or "phases" as identified in the accompanying bar graphs. Of interest are the W-rich regions in green and blue, where the W beam impacted. The discrete green and blue "fingers" arise from the different W isotopes due to their varying dispersion by the upstream analyzing magnet. The crosses indicate locations where XPS depth profiles of W concentrations were measured. (a) Total fluence: 1.75×10^{16} cm^{-2} (b) Total fluence: 3.5×10^{16} cm^{-2} (c) Total fluence: 7.0×10^{16} cm^{-2}.

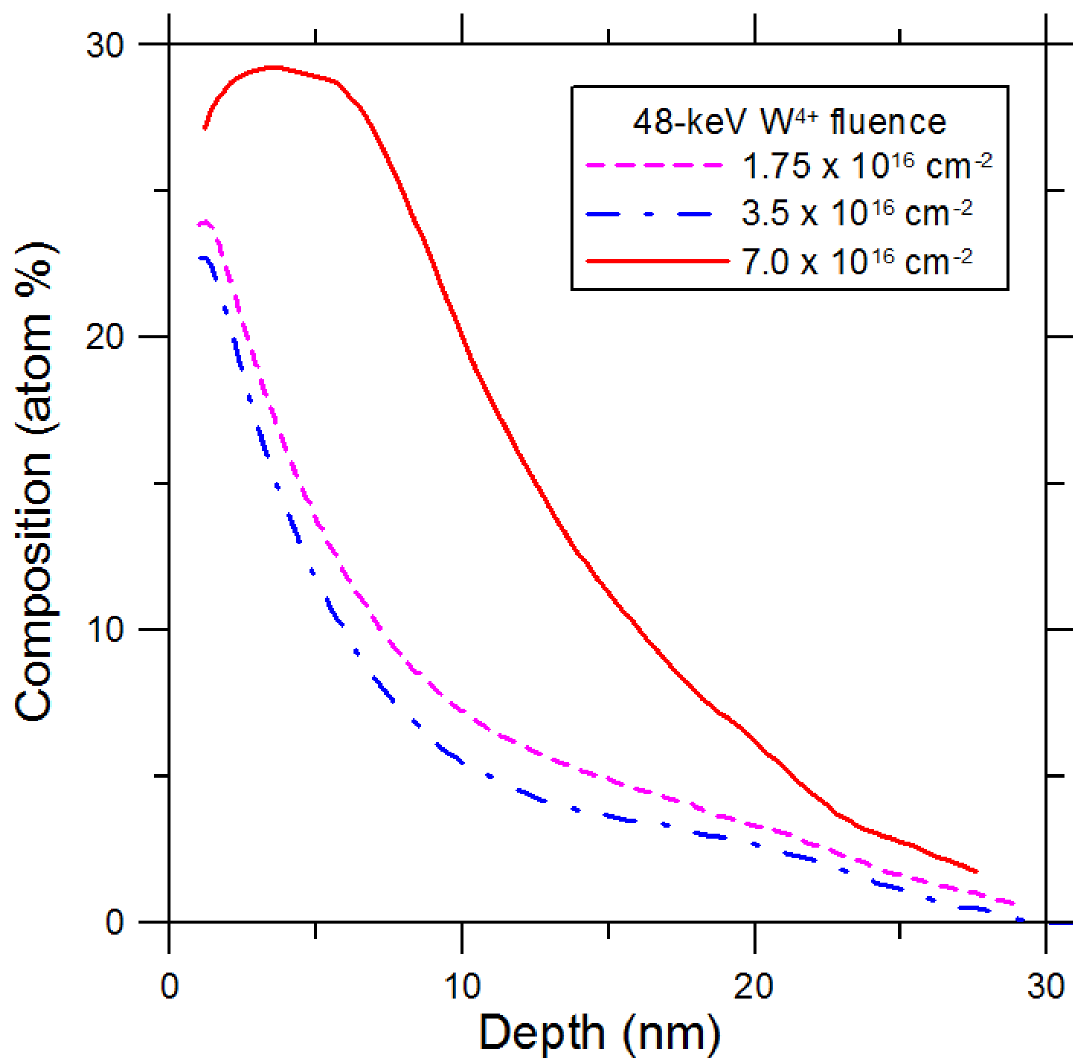

Figure 8. XPS depth profiles of W atom concentrations in PMMA targets exposed to 48-keV W^{4+} ions in the fixed configuration. Locations of the three measurements are indicated by the crosses in Figure 7.

(a)

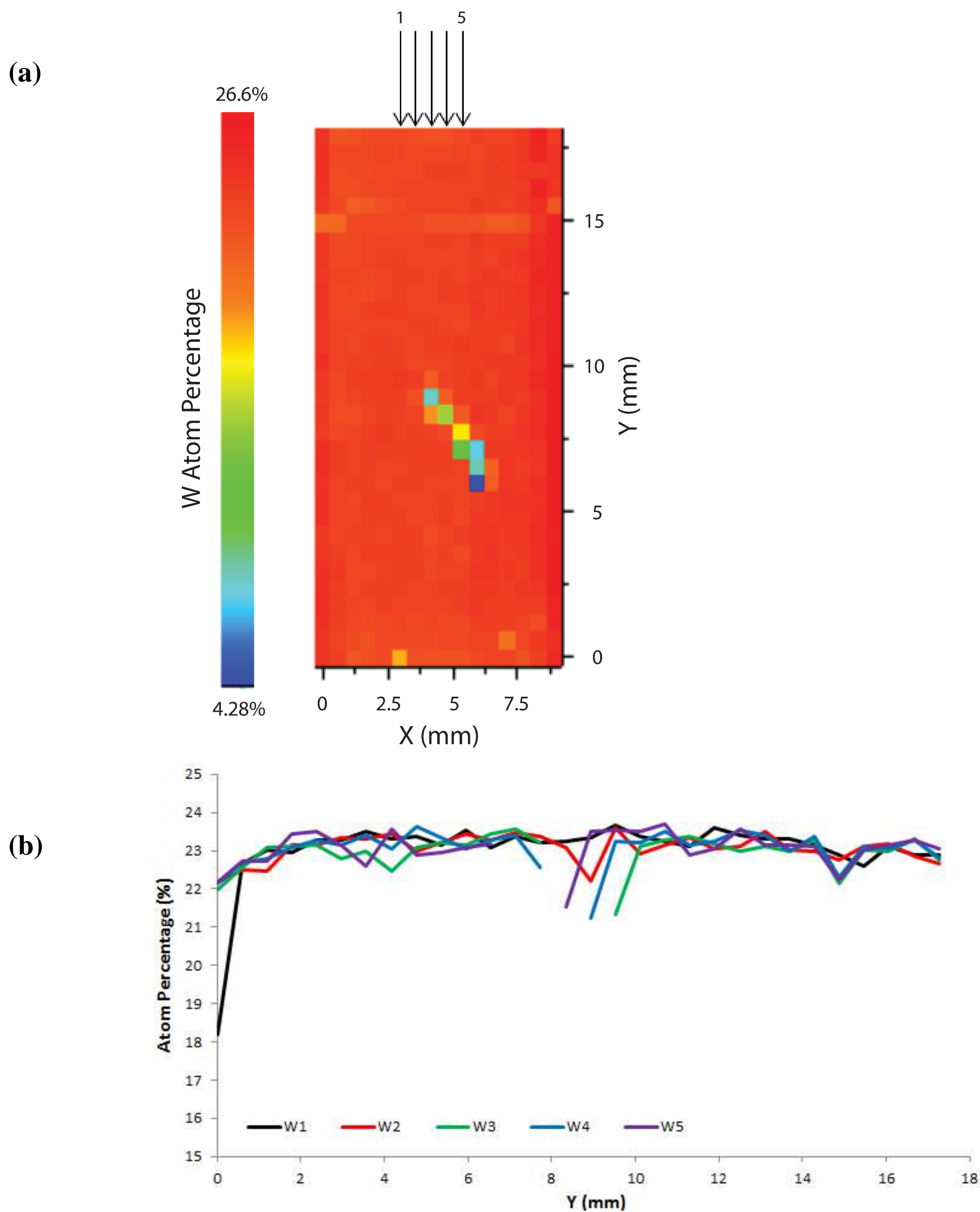

Figure 9. (a) Surface W composition of PMMA targets exposed to 48-keV W^{4+} ions in the rastered configuration (30 mm wide x 10 mm high raster area) as measured by the XPS technique. The W concentration is indicated by the color scale at left of the figure. (b) Tungsten atom percentage profiles along 5 vertical scans (indicated by arrows in (a)) through the XPS analysis area. Apparent non-uniformity in the center of (a) and (b) is due to inadvertent surface damage produced during sample removal from the implantation chamber.

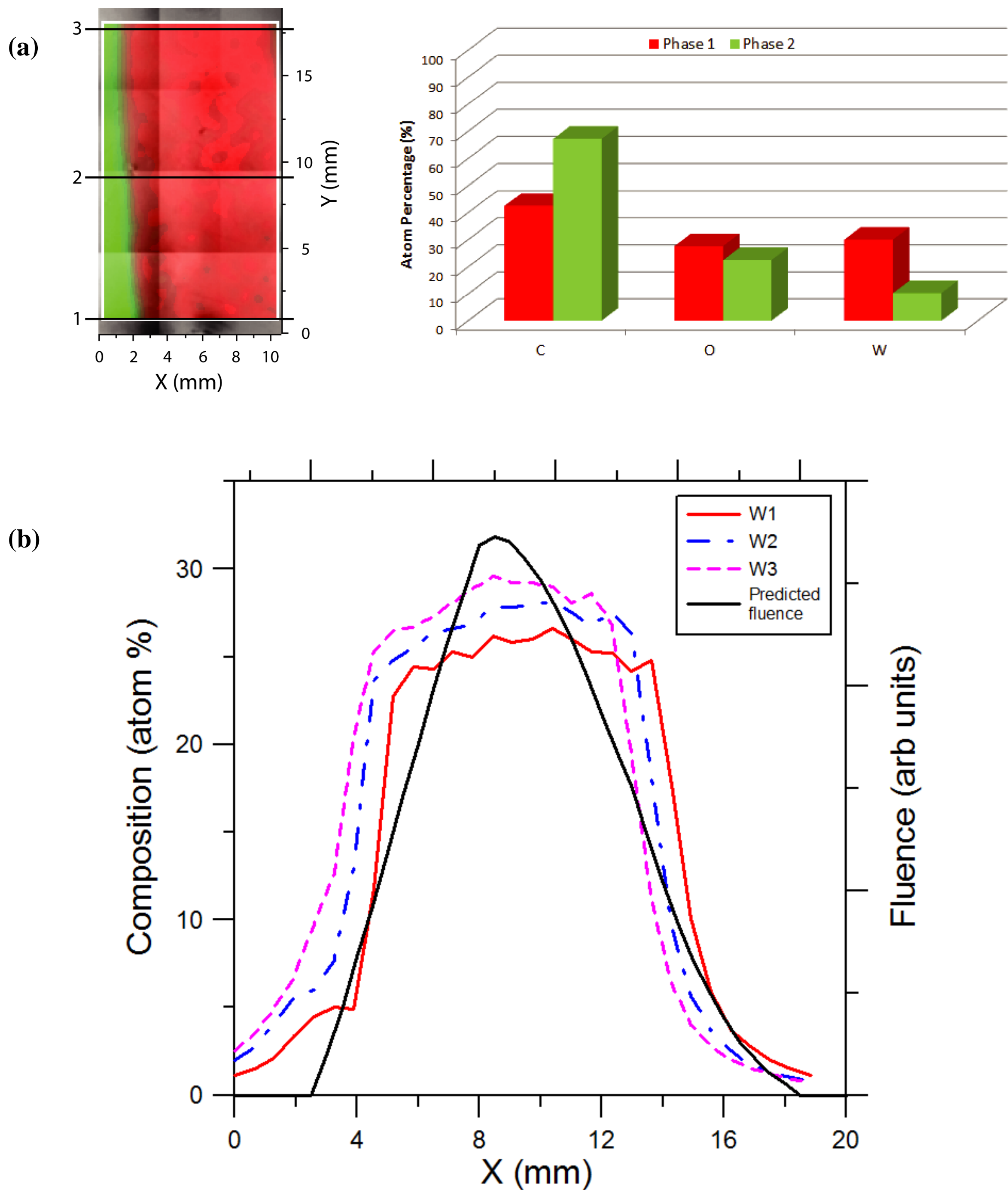

Figure 10. (a) Surface composition map of PMMA targets exposed to 4-keV W^{4+} ions in the rastered configuration (30 mm wide x 5 mm high raster area) as measured by the XPS technique. The 2 colors represent carbon-rich (green) and W-rich (red) regions (see phase histogram to right of map). (b) Tungsten atom percentage profiles along horizontal lines (indicated in (a)) through the XPS analysis area. Profile shape of fluence predicted by rastering simulations is shown for comparison as the solid black curve.

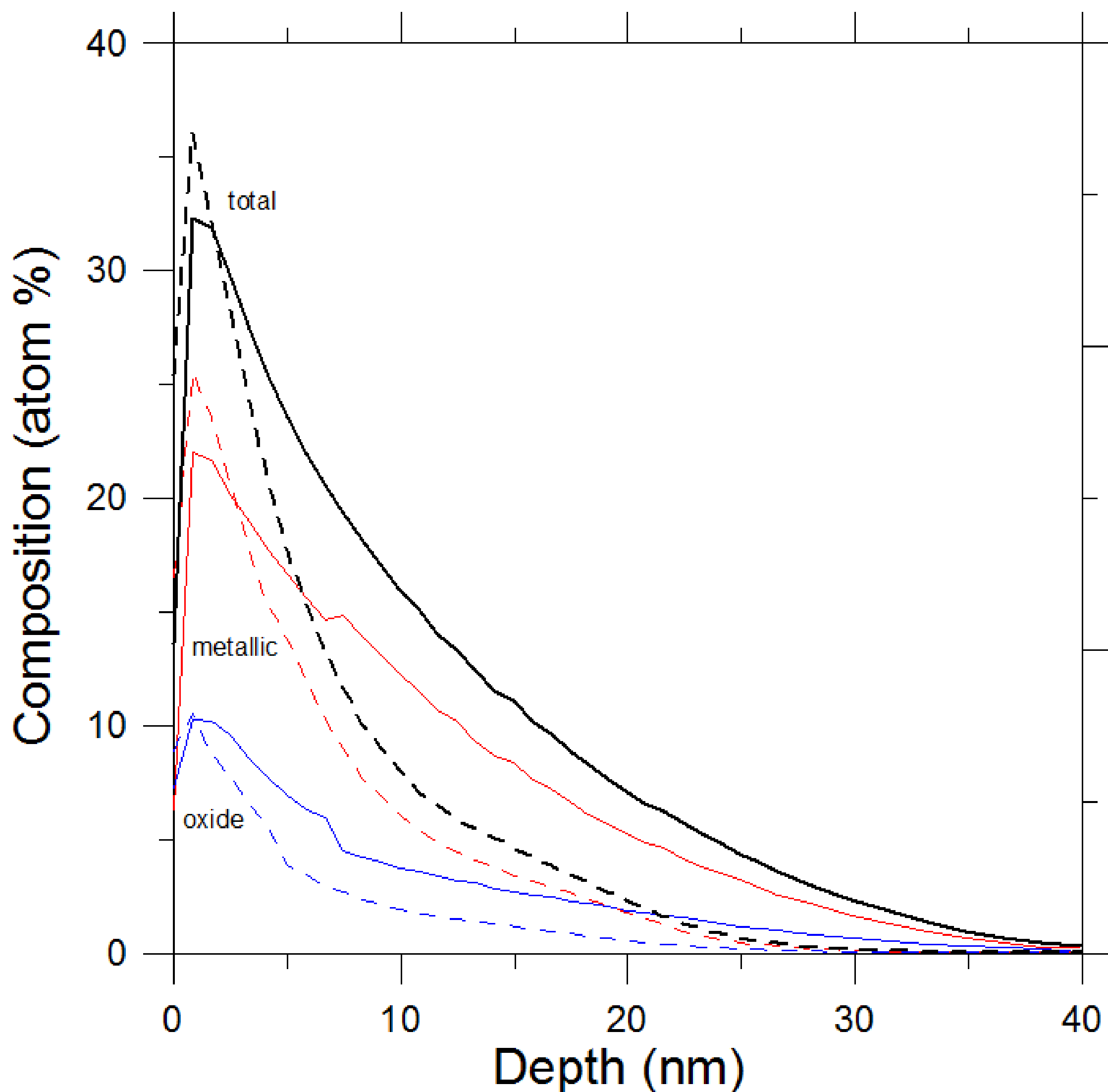

Figure 11. XPS depth profiles of W atom concentrations in PMMA targets exposed to 48-keV W^{4+} ions at two different locations in the raster area. The heavier (black) curves are for total W atom concentrations at the center (solid) and at a horizontal edge (dashed) of the raster area. The upper thin curves (red) represent the metallic-W concentration at the center (solid) and edge (dashed) locations, whereas the lower thin curves (blue) represent the oxide-W concentration and the center (solid) and edge (dashed) locations.

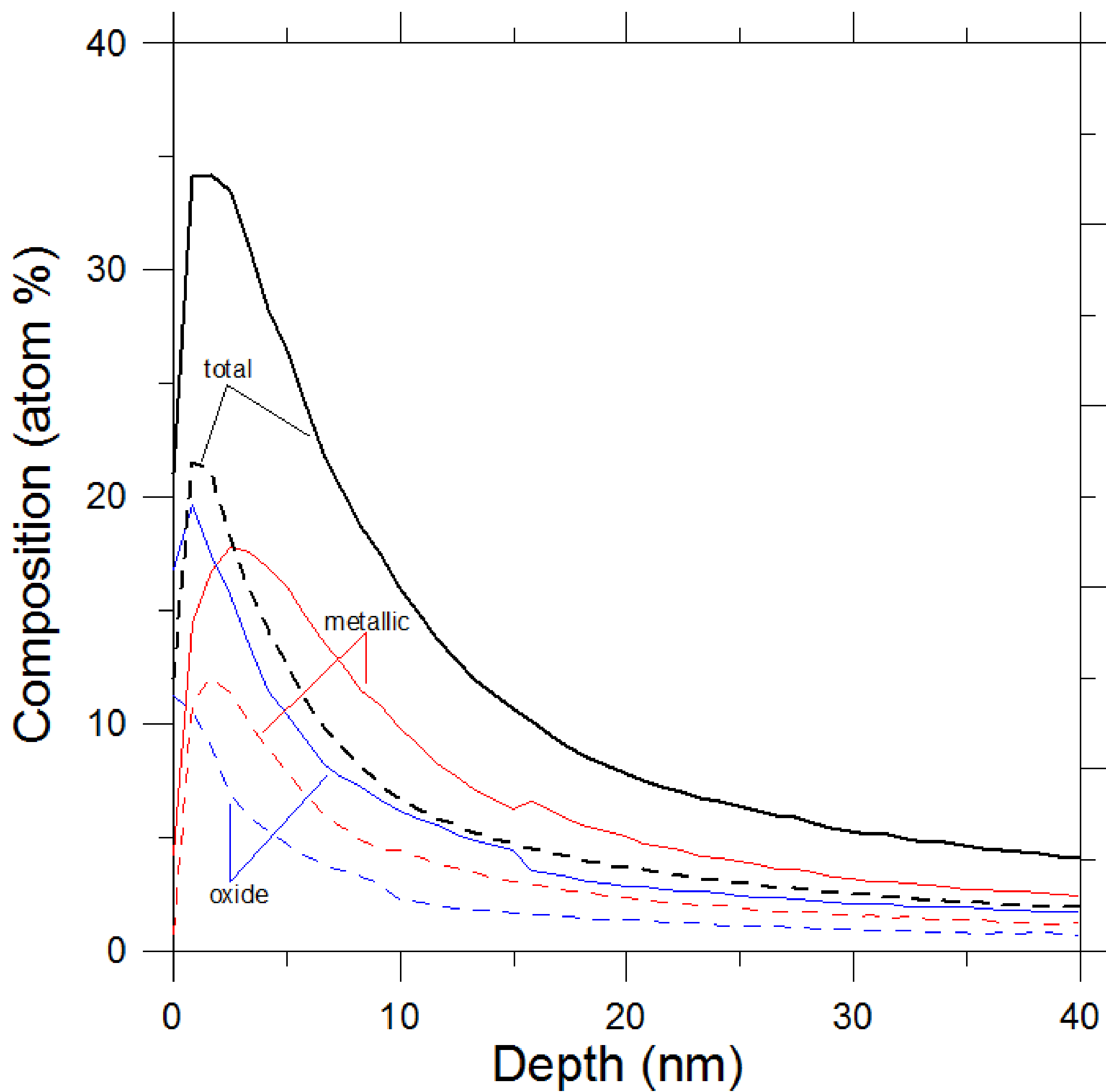

Figure 12. XPS depth profiles of W atom concentration in PMMA targets exposed to 4-keV W^{4+} ions at two different locations in the raster area. The heavier (black) curves are for total W atom concentrations at the center (solid) and at a horizontal edge (dashed) of the raster area. The broader-peaked thin curves (red) represent the metallic-W concentration at the center (solid) and edge (dashed) locations, whereas the narrower-peaked thin curves (blue) represent the oxide-W concentration and the center (solid) and edge (dashed) locations.